

Ballistic transport spectroscopy of spin-orbit-coupled bands in monolayer graphene on WSe₂

Qing Rao^{1#}, Wun-Hao Kang^{2#}, Hongxia Xue¹, Ziqing Ye³, Xuemeng Feng³, Kenji Watanabe⁴, Takashi Taniguchi⁴, Ning Wang³, Ming-Hao Liu^{2*} & Dong-Keun Ki^{1*}

¹Department of Physics, The University of Hong Kong, Pokfulam Road, Hong Kong, China

²Department of Physics, National Cheng Kung University, Tainan 70101, Taiwan

³Department of Physics and Center for Quantum Materials, The Hong Kong University of Science and Technology, Clear Water Bay, Kowloon 999077, Hong Kong, China

⁴National Institute for Materials Science, Namiki 1-1, Tsukuba, 305-0044, Ibaraki, Japan

#Equal contributions.

*Corresponding authors.

Email: minghao.liu@phys.ncku.edu.tw

Email: dkki@hku.hk

Spin-orbit coupling (SOC) provides unique capabilities to control spin by moving electrons around or turn electron trajectories by rotating spin. Recently, van der Waals interactions with transition metal dichalcogenides was shown to induce strong SOC in graphene, offering great promises to combine large experimental flexibility of graphene with unique tuning capabilities of the SOC. Here, we investigate both SOC-driven band splitting and electron dynamics in monolayer graphene on WSe₂ by measuring ballistic transverse magnetic focusing (TMF) effect. We found the splitting in the first focusing peak whose evolution in charge density and magnetic field is well reproduced by calculations using the SOC strength of ~13 meV and its absence in the second peak due to interband scattering at the edge. Temperature dependence measurement shows the possible suppression of the electron-electron scattering in the system. Further, we found that

Shubnikov–de Haas oscillations exhibit SOC strength of ~3.4 meV, suggesting that it probes different electron dynamics, calling for new theory. In addition to providing spectroscopic evidence of the spin-orbit-coupled bands, our study demonstrates the possibility to exploit various ballistic transport effects in graphene, such as TMF, Veselago lensing, and Fabry-Pérot interference, to control or detect spin by turning ballistic electron motion.

Interfacial interactions with semiconducting transition metal dichalcogenides (TMDCs) have shown to be highly efficient to induce strong spin-orbit coupling (SOC) in graphene¹⁻³. For monolayer graphene, it was theoretically predicted to have two distinctive terms, one that couples out-of-plane spin and valley degrees of freedom (referred to as a spin-valley Zeeman term $\tau_z s_z$) and another that couples in-plane spin and sublattice degrees of freedom, similar to the Rashba term ($\tau_z \sigma_x s_y - \sigma_y s_x$), as follows.

$$H = H_0 + \Delta \sigma_z + \lambda \tau_z s_z + \lambda_R (\tau_z \sigma_x s_y - \sigma_y s_x), \quad (1)$$

where H_0 is the graphene's Dirac Hamiltonian, $\boldsymbol{\sigma} = (\sigma_x, \sigma_y, \sigma_z)$ is a Pauli matrix vector that acts on the sublattice degree of freedom in graphene, $\boldsymbol{s} = (s_x, s_y, s_z)$ is a Pauli matrix vector that acts on spin, and $\tau_z = \pm 1$ identifies two different valleys in graphene ($\Delta \approx 0$ due to a large lattice mismatch between the graphene and TMDCs)^{2,4,5}. Both SOC terms induce band splitting in graphene and their strengths (λ and λ_R) can be further tuned by an electric field perpendicular to the layers⁶⁻¹⁰ or by pressure¹¹.

Combined with high electron mobility and large experimental flexibility of graphene, such a strong interface-induced SOC makes the graphene on TMDCs ideal for ballistic spintronics where ballistic electron motion can be used to control or detect electron spin¹²⁻¹⁷. It is particularly interesting as graphene has shown pronounced ballistic transport effects with large tunability, such as transverse magnetic focusing (TMF)¹⁸⁻²⁰, Veselago lensing^{21,22}, and Fabry-Pérot interference^{23,24} among many others. They have

also shown unique features originating from the relativistic nature of Dirac electrons¹⁸⁻²⁴. However, a vast number of the previous studies have focused on detecting spin relaxation due to electron scattering rather than the ballistic motion^{1-3,11,25-30}. Moreover, only few studies have found a direct evidence for the SOC-induced band splitting by measuring beatings in Shubnikov-de Hass (SdH) oscillations (for both mono- and bilayer graphene)^{3,8,10,31} or tracing changes in quantum capacitance (for bilayer graphene only)⁹. Not only to understand the effect of the SOC on the electronic properties of the system such as the band topology^{32,33} but also to exploit its full potential on ballistic spintronics¹²⁻¹⁷, it is therefore essential to demonstrate the ballistic transport in graphene on TMDCs while simultaneously probing their band structures and electron dynamics.

To fill this missing link, we employ TMF technique in monolayer graphene on WSe₂ as it can not only probe the SOC-induced band splitting but also investigate electron dynamics simultaneously (see **Figs. 1a,b**). TMF occurs when ballistic carriers injected from a narrow aperture (“injector”) at the edge of the sample are subject to a small perpendicular magnetic field ($\mathbf{B} = B\hat{z}$)³⁴. Owing to the Lorentz force, the carriers follow skipping cyclotron orbits and focus on another narrow aperture (“collector”) at a distance (L) that equals an integer multiple of $2r_c$ with a cyclotron radius $r_c = \hbar k_F / eB$, where \hbar is the reduced Planck constant, k_F is the Fermi momentum, and e is the elementary charge. Upon sweeping magnetic fields, the collector voltage will exhibit a set of resonance peaks at certain B -values determined by k_F ,

$$B_j = \pm \frac{2j\hbar}{|e|L} k_F, \quad (2)$$

where j is an integer and \pm represents electron and hole for the configuration shown in **Fig. 1a**). This enables the detection of Fermi surface configurations³⁴⁻³⁶. In the systems with multiple bands¹⁸, for instance, there will be multiple sets of resonance peaks at different B -values from which one can deduce their band structures. Moreover, TMF

can also be used to study or control electron dynamics as charge carriers follow skipping cyclotron orbits during the process. In 2D electron gas (2DEG) systems with SOC, the TMF was indeed used to probe spin-orbit split bands and extract SOC strength by studying the separation of the peaks^{12,14,16}, deduce spin polarization by comparing their heights¹², or focus spin-polarized current by controlling ballistic electron motion^{12,14,15}. **Fig. 1b** shows the energy band structure of the monolayer graphene on WSe₂ calculated using the Hamiltonian Eq. (1) that exhibits two spin-orbit split bands, S_+ and S_- , and the simulated two-point conductance spectra exhibiting multiple focusing peaks (see **Supplementary Information** for simulation details^{37,38}).

To study the ballistic TMF effect, we used a dry pick-up and transfer technique to assemble a stack of hexagonal boron-nitride (h-BN), monolayer graphene, and multilayer WSe₂ such that the graphene is protected from the harsh chemical environments in the following nanofabrication process³⁹. Standard electron beam lithography and lift-off were carried out to make Hall bar devices on 285-nm-thick SiO₂ substrate with doped silicon underneath used as a gate to control charge density n (see **Fig. 1a** and **Supplementary Information** for fabrication details). Electron transport through the fabricated devices was measured in a 1.5 K variable temperature insert with 14-T superconducting magnet using a standard low-frequency AC lock-in technique (see **Supplementary Information**). **Fig. 1c** shows the carrier density dependences of the four-probe resistances of two different samples 1 and 2 measured at 1.5 K, exhibiting high quality with carrier mobility of 200,000 ~ 400,000 cm²V⁻¹s⁻¹. Especially on the hole side, the symmetry broken quantum-Hall states were observed at magnetic fields as low as ~3 T (marked by black triangles in **Fig. 1d**). This indicates higher hole mobility in our sample than on the electron side, which is consistent with the observation of the larger negative non-local Hall resistance $R_{ae,bf}$ on the hole side (the inset of **Fig. 1c**) originating from the ballistic electron motion⁴⁰ ($R_{\alpha\beta,\gamma\delta} \equiv V_{\gamma\delta}/I_{\alpha\beta}$ refers to the resistance measured by sending a current from contact α to β and

measuring voltage between contacts γ and δ). Having such a high mobility—equivalently, a long mean free path—is important to resolve the small splitting of the focusing peak expected theoretically (**Fig. 1b**, right).

The TMF signal ($R_{nl} = V_{cj}/I_{ai}$) is measured in a non-local configuration upon varying n and B as depicted in **Fig. 1a**. **Figs. 2a,b** show the resulting maps of $R_{nl}(n, B)$ from the sample 1 and 2, respectively. Both exhibit similar TMF spectra and their evolutions in n and B . Overall, the positions of the j -th TMF peak in B follow the Eq. (2) with $k_F = \sqrt{\pi|n|}$, as expected for monolayer graphene. However, on the hole side (where we found the higher sample quality), we can clearly identify the splitting of the first focusing peak that evolves continuously in n and B and no splitting in the second (here, we only focus on the peaks that appear in all density range). **Fig. 2c** and the right panel of **Fig. 2b** further magnify the features by plotting 1D cuts $R_{nl}(B)$ of the map at different n which qualitatively matches the simulation result shown in **Fig. 1b**. Moreover, different from TMF measurement on pristine monolayer graphene¹⁸, we found a large TMF signal constantly exceeding 100Ω around zero density (nearly two orders of magnitude larger than the values at finite densities; see the dark red bands near zero density in the color maps shown in **Figs. 2a,b**).

All features found in the experiment (**Figs. 2a,b**) match well with our expectations for the graphene with SOC. First, the first focusing peak splits due to the SOC-induced multiple bands S_+ and S_- in our sample (**Fig. 1b**). Note that no such a prolonged splitting in both n and B was observed in other graphene systems without SOC¹⁸⁻²⁰. Moreover, we were able to fit the positions of the first focusing peaks with calculations using the SOC strength of $\sqrt{\lambda^2 + \lambda_R^2} = 13.0 \pm 4.7$ meV for both samples as marked by black dotted lines in **Figs. 2a,b**. **Figs. 2d,e** further emphasize the accuracy of the fitting by plotting the average of the normalized difference between the data and the calculation $\langle \delta B^2 \rangle$ as a function of λ and λ_R in a color scale (a darker color indicates the

smaller $\langle \delta B^2 \rangle$ so the better fitting; see the caption for more details). We note that the fitting works for any values of λ and λ_R as long as they satisfy $\sqrt{\lambda^2 + \lambda_R^2} = 13.0 \pm 4.7$ meV, indicating that the λ and λ_R has a similar effect on the TMF peak splitting—equivalently, the band splitting—in the density range we studied. This is expected as in the density range explored (i.e., when the Fermi energy is larger than λ and λ_R), both λ and λ_R gives an identical splitting in momentum, $\Delta k = 2\sqrt{\lambda^2 + \lambda_R^2}/\hbar v_F$ with Fermi velocity $v_F \approx 10^6$ m/s. This is consistent with the previous SdH oscillations measurements that probe electron bands^{3,31}.

In addition, we found that the amplitude of the first split peak near zero B is always lower than that of the second (see, e.g., **Fig. 2c**). Interestingly, it was found and expected in 2DEG systems with Rashba SOC when adiabatic transitions between the quantized sub-bands at the injector with width w polarize electron spin⁴¹. Slightly modifying the condition derived for 2DEG⁴¹, we get $\frac{\Delta k}{2k_F} > \frac{3}{16} \left(\frac{\lambda_F}{w}\right)^2 \rightarrow \lambda_R > \frac{3\pi}{8} \frac{\hbar v_F \lambda_F}{w^2} \approx 0.25 \sim 0.35$ meV for our sample with Fermi wavelength $\lambda_F \approx 30 \sim 40$ nm, and $w \approx 300$ nm. The SOC strengths estimated in our study are well in the range (**Figs. 2d,e**). On the other hand, in graphene on TMDCs, it was predicted that the characteristic spin winding of the spin-orbit-coupled bands leads to a current-induced spin polarization⁴² which can result in the uneven heights of the two first focusing peaks.

Furthermore, the absence of the splitting in the second peak can be interpreted as the mixing of the spin-orbit-coupled bands S_{\pm} when the carriers scatter at the sample edge. Due to this mixing, the carrier can be transferred from one band S_+ (or S_-) to another S_- (or S_+) which leads to a single peak as illustrated in the bottom inset of **Fig. 2a**. To confirm this origin, we have further calculated electron trajectories for the second peak with and without the inter-band transition at the edge in **Fig. S1**. As expected, without the inter-band mixing, the second focusing peak also exhibits splitting. Similar behavior has been observed and discussed in 2DEG systems with SOC^{14,16,43}. Lastly, we can also

explain the observed large R_{nl} near zero density (**Figs. 2a,b**) as the presence of the spin Hall effect (SHE)¹ in the system. From the very weak temperature dependence of the conductance minimum at zero density (**Fig. 3a**), we first confirm that this is not from the gap opening at charge neutrality which may have given a large TMF signal as found in the gapped trilayer graphene¹⁸. In contrast, we found a large non-local Hall signal near charge neutrality point that exceed the ohmic contribution by about 230 Ω (**Fig. 3b**). This is consistent with SHE found in a similar system previously¹. All features found in the TMF spectra (**Figs. 2a-c**) can, therefore, be captured by the interface induced SOC in graphene on WSe₂.

We now examine temperature dependence of the TMF spectra in **Figs. 3c,d** to study the electron dynamics in the system. Upon increasing temperature, we have found that the amplitude of the TMF spectra decreases (**Fig. 3c**). Following the previous studies^{19,20}, we determined the total area below the first focusing peaks A_1 at varying temperatures from 1.5 K to 300 K and calculated the relative scattering length from $L_S/L_0 = (\ln [(A_1(1.5K)/A_1(T))])^{-1}$, which is proportional to the effective scattering time (L_0 is the length of the semi-circular electron trajectory corresponding to the first focusing peak). **Fig. 3d** shows the result exhibiting a clear $T^{-1.8}$ dependence on both electron and hole side for different charge densities. This is between electron-phonon scattering (T^{-1}) and electron-electron ($e-e$) scattering (T^{-2}), indicating that the WSe₂ may have screened $e-e$ interactions due to its large dielectric constant ($\epsilon_0 \approx 7.9$) compared with hBN ($\epsilon_0 \approx 3.8$)⁴⁴. This suggests a possibility to use the WSe₂ to suppress $e-e$ collision phenomena such as the viscous electron flow⁴⁵ and study the effects when the SOC is present.

To further elucidate the band splitting in our system, we measured SdH oscillations at higher magnetic field range. The results are summarized in **Fig. 4**. In all the density range including the electron side, we found beatings in the oscillations originating from

the spin-orbit-coupled split bands (**Fig. 4b**). For quantitative analysis, we performed fast Fourier transforms (FFT) and extracted the frequency f at which the spectra exhibit a peak (**Fig. 4a**) which is directly connected to the area of the corresponding Fermi surface by $f = nh/2e$ and $n = k_F^2/2\pi$ assuming broken spin degeneracy due to SOC. It can therefore be used to estimate the SOC strengths independently. **Fig. 4c** shows the result (we have selected the peaks that evolve continuously in density only) which shows a good agreement with the calculation using the SOC strengths along the circle $\sqrt{\lambda^2 + \lambda_R^2} = 3.4 \pm 0.7$ meV (**Fig. 4d**). This is about 4 times smaller than those extracted from the TMF data (**Figs. 2d,e**), indicating that the TMF and SdH oscillations probe different electron dynamics.

To compare the results more directly, we have calculated $\Delta B_{SdH} = (2\hbar/|e|L)|k_{F1} - k_{F2}|$, the splitting of the first TMF peak in B using the k_F -values extracted from the SdH oscillations (**Fig. 4c**) and plotted the splitting measured in TMF, ΔB_{TMF} (extracted from **Figs. 2a-c**), together. As shown in **Fig. 4e**, ΔB_{TMF} remains larger than ΔB_{SdH} in all density range accessed in the experiment. Interestingly, we found that the similar behavior was observed in 2DEG systems with SOC^{14,16} where it was suggested¹⁶ that there might be a SOC term, such as a linear- k term, that does not affect the total area of the Fermi surface by enlarging one semicircle of the surface and reducing the other simultaneously. This is possible because the SdH oscillation requires carriers to complete a full cyclotron motion while in TMF, they only make a half turn in the Fermi surface. Therefore, if there is the SOC term that shifts the Fermi surface in one momentum direction, it may be possible that one finds larger splitting in TMF than in SdH as seen experimentally. However, it is also possible that the SdH oscillations require relatively large magnetic fields to form Landau levels which can induce non-negligible Zeeman energy and may affect the spin-valley Zeeman and Rashba terms in Eq. (1) differently (see **Supplementary Information** for more discussions). Although more studies are required to understand this discrepancy, our measurement shows that

the behaviour occurs not only in semiconductor heterostructures-based 2DEG systems^{14,16} but also in graphene when SOC exists. Therefore, it is likely that there is a fundamental origin behind this phenomenon.

In **Fig. 4d**, we also include all SOC strengths extracted from the previous measurements on monolayer graphene-TMDC heterostructures for comparison. Overall, the relaxation time analysis from weak anti-localization or spin-Hall effect measurements^{1,25,26,30} shows a large sample-to-sample variation (**Fig. 4d**). It can be from the fact that these measurements rely on the model to connect the spin relaxation process in the system with the SOC strength, which is sensitive to the sample-specific electron scattering process³⁰. On the other hand, TMF and SdH oscillations directly probe the size of the Fermi surface, which can be compared with theoretically calculated band structures without considering details of the scattering processes. The recent study on SdH oscillation in monolayer graphene-WSe₂ heterostructures³¹ has indeed shown a SOC strength $\sqrt{\lambda^2 + \lambda_R^2} = 2.51$ meV close to ours (**Fig. 4d**). Moreover, in our TMF study, we found similar SOC strengths in two different samples (**Figs. 2d,e**). This further elaborates the benefits of carrying out the (ballistic) transport spectroscopy on understanding electronic properties of the system with SOC.

Our work demonstrates that graphene on TMDCs can support ballistic transport that can be used not only to gain more insights of the microscopic electron process in the system but also to exploit various ballistic transport effects that are pronounced in graphene. It is particularly interesting as, in contrast to the existing studies on graphene spintronics^{17,46,47}, TMF separates spin-up and spin-down carriers in real space. This enables detection and measurement of both spins independently, instead of only the majority one injected from magnetic contacts. This, therefore, offers an alternative venue for graphene spintronic applications^{17,46,47}. The similar strategies can also be used to study other 2D materials or heterostructures with strong SOC, such as bilayer

graphene-TMDC heterostructures⁸⁻¹⁰, black phosphorus⁴⁸, and more, which will offer new understandings about the effect of SOC in these material systems.

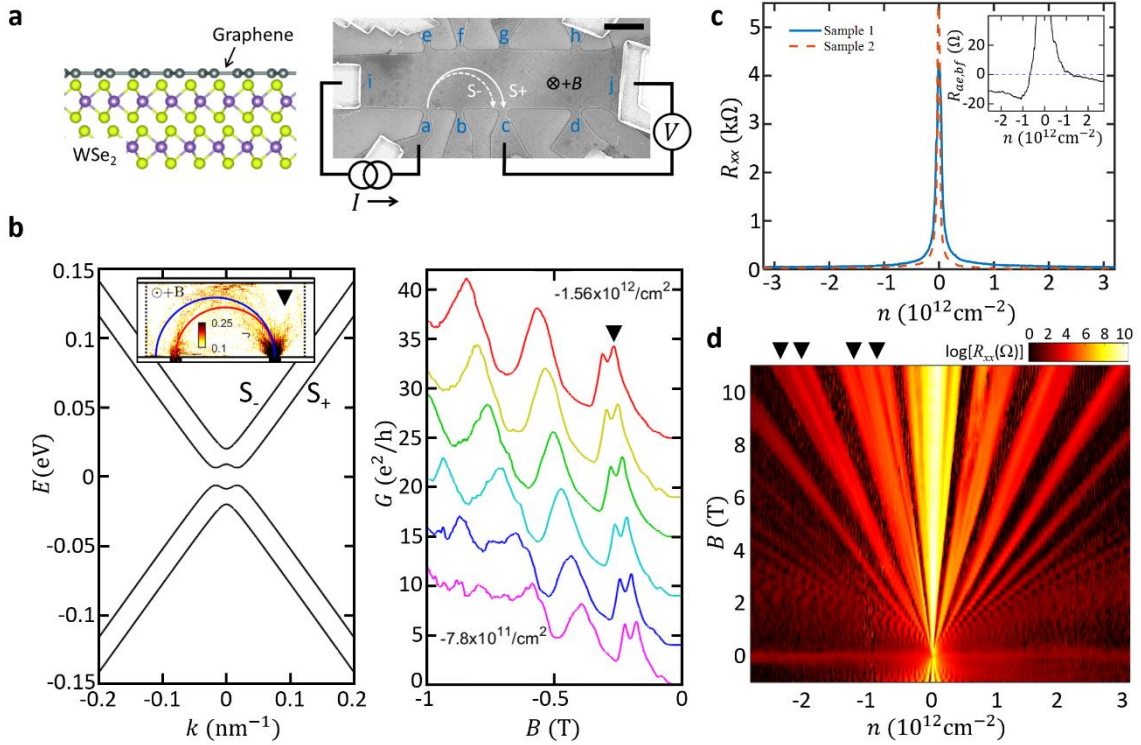


Figure 1. Sample characteristics and TMF measurement scheme. **a**, The schematic of monolayer graphene-multilayer WSe₂ heterostructures (left) and scanning electron microscope image of the device with a TMF measurement configuration (right; a scale bar: 2 μm). The two semicircles (S_±) on the right illustrate trajectories of the carriers at different spin-orbit-coupled bands S_± shown in **b** under perpendicular magnetic field B. **b**, The energy dispersion of graphene on WSe₂ derived from the effective Hamiltonian Eq. (1) in the main text (left) using SOC strengths of $\lambda = \lambda_R = 8.9$ meV ($\sqrt{\lambda^2 + \lambda_R^2} = 12.5$ meV), and the corresponding TMF spectra at 6 different hole densities, n (in 10¹² cm⁻²) = -0.78, -0.93, -1.09, -1.24, -1.40, and -1.56 (from bottom to top) calculated from the tight-binding model (right). The inset on the left shows the simulated local current density map at the focusing peak marked by a down triangle on the right. **c**, The carrier

density (n) dependence of the four-probe resistances R_{xx} of two different samples 1 (blue solid line) and 2 (red broken line) measured at 1.5 K. Both exhibits a sharp resistance peak at zero density, indicating high device quality. The inset shows the non-local Hall resistance $R_{ae,bf}(\equiv V_{bf}/I_{ae})$, exhibiting a large negative signal on the hole side originating from the ballistic transport. **d**, The Landau fan—the $\log(R_{xx})$ as a function of n and B —plotted in a color scale (the darker color corresponds to the lower resistance), showing high-quality quantum Hall effect measured at 1.5 K. On the hole side, the broken-symmetry states begin to appear at ~ 3 T (indicated by black down-triangles) which indicates higher quality on the hole side, consistent with the large negative $R_{ae,bf}$ on the hole side shown in the inset of **c**.

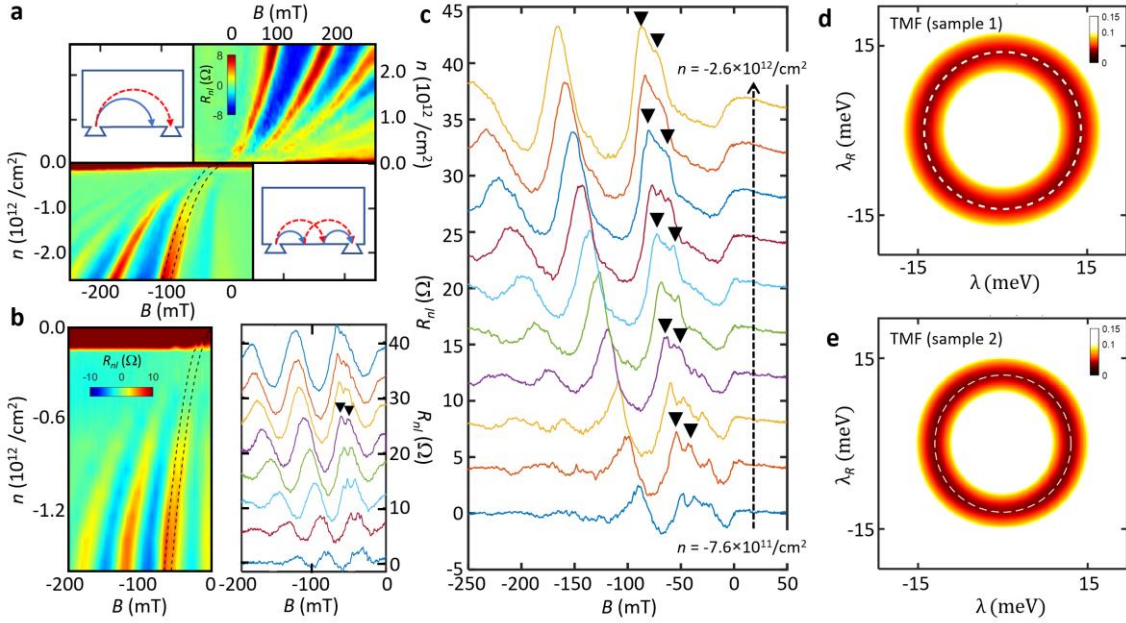


Figure 2. TMF spectra. **a**, Color-scale maps of TMF signal $R_{nl}(B, n)$ measured in sample 1 at 1.5 K (top right: electron side; bottom left: hole side). The broken lines show the theoretically calculated focusing peaks at $\sqrt{\lambda^2 + \lambda_R^2} = 13.9$ meV. Inset: carrier trajectories for the first and second focusing peaks (top left and bottom right, respectively). **b**, TMF map and the corresponding 1D cuts measured in sample 2 at 1.5

K. The broken line shows the theoretically calculate focusing peaks at $\sqrt{\lambda^2 + \lambda_R^2} = 12.0$ meV. **c**, 1D cuts of the data from the sample 1 shown in **a**. The black down-triangles in **b** and **c** mark some of the two split peaks for guidance. **d-e**, The color-scale map of the average difference $\langle \delta B^2 \rangle \equiv \sum [(\Delta B_+/B_0)^2 + (\Delta B_-/B_0)^2]/N$ as a function of λ and λ_R from the sample 1 and 2, respectively (N : number of data used). ΔB_{\pm} is the difference between the predicted focusing peak positions from the simulation for certain (λ, λ_R) and the real peak positions measured in the experiment for the band S_{\pm} , whereas B_0 is the half of the maximum splitting observed. Thus, the smaller $\langle \delta B^2 \rangle$ (darker in the map) indicates a better agreement. The best-fit value is drawn by a dashed white circle. We use a criterion $\langle \delta B^2 \rangle \leq 0.1$ to extract the SOC strengths of $\sqrt{\lambda^2 + \lambda_R^2} = 13.9 \pm 4.0$ meV and 12.0 ± 3.5 meV, for sample 1 and 2 respectively.

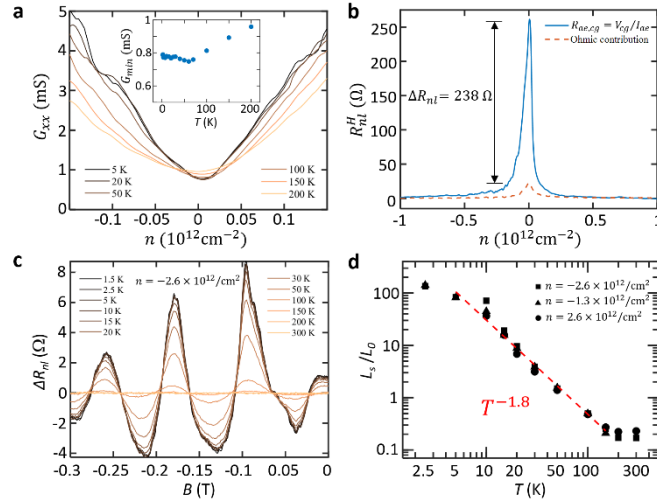


Figure 3. Temperature dependence measurements. **a**, Temperature dependence of the local four-terminal conductance $G_{xx} = 1/R_{xx}$ as a function of charge density, exhibiting a weak temperature dependence of the minimum conductance G_{min} at zero density as magnified in the inset. **b**, Non-local Hall resistance $R_{ae,cg}$ as a function of carrier density n (blue solid line) compared with the calculated Ohmic contribution (red broken line)¹. Large non-local Hall signal is consistent with the spin Hall effect

observed in a similar system¹. **c**, Temperature dependence of the TMF spectra at $n = -2.6 \times 10^{12} \text{ cm}^{-2}$. The smooth backgrounds are extracted by a Gaussian filter with a full width at half maximum of 0.2 T, which is larger than the oscillation period of TMF signals. **d**, The relative scattering lengths (calculated from areas below the first focusing peaks) at $n = -2.6 \times 10^{12} \text{ cm}^{-2}$ (square), $n = -1.3 \times 10^{12} \text{ cm}^{-2}$ (triangle), and $n = 2.6 \times 10^{12} \text{ cm}^{-2}$ (circle) as a function of temperature plotted in a log scale, which follows the $T^{-1.8}$ dependence, indicated by the dashed red line. See the main text for more discussions.

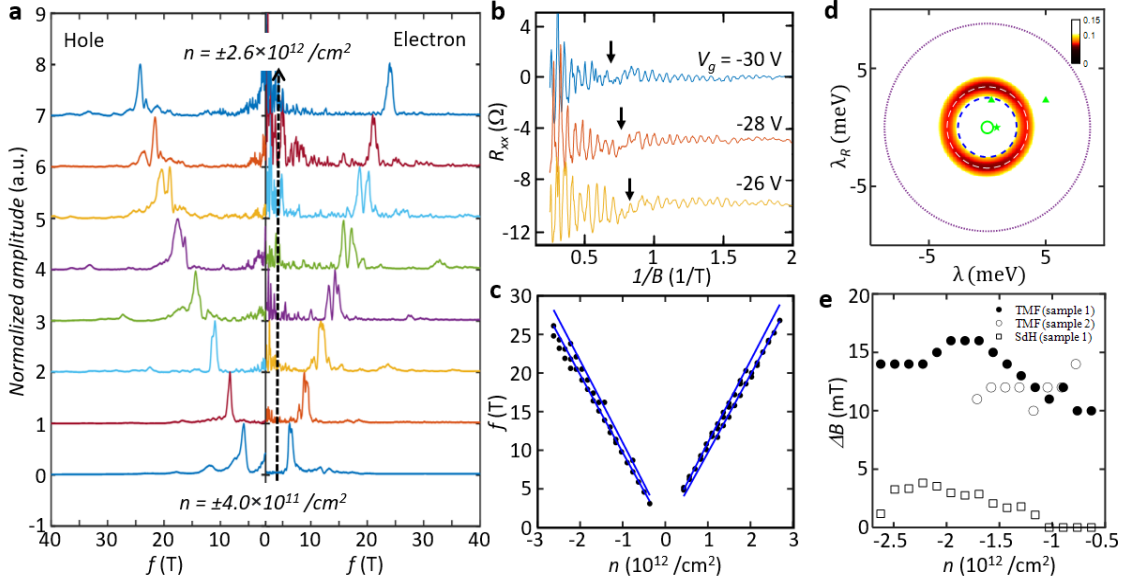


Figure 4. SdH oscillations. **a**, The FFT spectra derived from the SdH oscillation curves as a function of carrier density n , for both electron and hole side. **b**, Representative SdH oscillation curves, which clearly show the beating patterns (marked by arrows; curves are vertically offset for clarity). **c**, The frequency peak positions extracted from the FFT spectra at different carrier densities (see **Supplementary Information**). The solid lines show the fitting with calculated band structures using $\sqrt{\lambda^2 + \lambda_R^2} = 3.4 \text{ meV}$. **d**, The color-scale map of the average difference $\langle \delta B^2 \rangle$ in λ and λ_R from the SdH oscillations

with the best fit value drawn by dashed white circle (see the caption of **Figs. 2d-e** for details). Using $\langle \delta B^2 \rangle \leq 0.1$, we get $\sqrt{\lambda^2 + \lambda_R^2} = 3.4 \pm 0.7$ meV. The values from the previous studies are included for comparison: a dotted purple circle from spin Hall effect¹, a dashed blue circle from SdH oscillations³¹, and circle²⁵, square²⁶, and two filled green triangles³⁰ (two different values are obtained from different spin relaxation mechanisms) from weak anti-localization measurements. Some studies^{1,25,26} used $\lambda/2$ and $\lambda_R/2$ in the Hamiltonian Eq. (1), so we divided the values by half in the plot. **e**, The splitting of the first TMF peak in B (ΔB_{TMF}) at different charge densities extracted from **Fig. 2** compared with the predicted ΔB calculated from the SdH oscillations (ΔB_{SdH} ; **c**). Over the whole density range, the ΔB_{SdH} remains smaller than the ΔB_{TMF} .

References

- 1 Avsar, A. *et al.* Spin-orbit proximity effect in graphene. *Nat. Commun.* **5**, 4875 (2014).
- 2 Wang, Z. *et al.* Strong interface-induced spin-orbit interaction in graphene on WS₂. *Nat. Commun.* **6**, 8339 (2015).
- 3 Wang, Z. *et al.* Origin and Magnitude of 'Designer' Spin-Orbit Interaction in Graphene on Semiconducting Transition Metal Dichalcogenides. *Phys. Rev. X* **6**, 041020 (2016).
- 4 Gmitra, M. & Fabian, J. Graphene on transition-metal dichalcogenides: A platform for proximity spin-orbit physics and optospintronics. *Phys. Rev. B* **92**, 155403 (2015).
- 5 Zubair, M., Vasilopoulos, P. & Tahir, M. Influence of interface induced valley-Zeeman and spin-orbit couplings on transport in heterostructures of graphene on WSe₂. *Phys. Rev. B* **101**, 165436 (2020).
- 6 Khoo, J. Y., Morpurgo, A. F. & Levitov, L. On-Demand Spin-Orbit Interaction from Which-Layer Tunability in Bilayer Graphene. *Nano Lett.* **17**, 7003-7008 (2017).
- 7 Gmitra, M. & Fabian, J. Proximity Effects in Bilayer Graphene on Monolayer WSe₂: Field-Effect Spin Valley Locking, Spin-Orbit Valve, and Spin Transistor. *Phys. Rev. Lett.* **119**, 146401 (2017).
- 8 Afzal, A. M. *et al.* Gate Modulation of the Spin-orbit Interaction in Bilayer Graphene Encapsulated by WS₂ films. *Sci. Rep.* **8**, 3412 (2018).
- 9 Island, J. O. *et al.* Spin-orbit-driven band inversion in bilayer graphene by the van der Waals proximity effect. *Nature* **571**, 85-89 (2019).
- 10 Wang, D. *et al.* Quantum Hall Effect Measurement of Spin-Orbit Coupling Strengths in Ultraclean Bilayer Graphene/WSe₂ Heterostructures. *Nano Lett.* **19**, 7028-7034 (2019).

- 11 Fülöp, B. *et al.* Boosting proximity spin–orbit coupling in graphene/WSe₂
heterostructures via hydrostatic pressure. *npj 2D Mater. Appl.* **5**, 82 (2021).
- 12 Rokhinson, L. P., Larkina, V., Lyanda-Geller, Y. B., Pfeiffer, L. N. & West, K.
W. Spin Separation in Cyclotron Motion. *Phys. Rev. Lett.* **93**, 146601 (2004).
- 13 Frolov, S. M. *et al.* Ballistic spin resonance. *Nature* **458**, 868–871 (2009).
- 14 Lo, S.-T. *et al.* Controlled spatial separation of spins and coherent dynamics in
spin-orbit-coupled nanostructures. *Nat. Commun.* **8**, 15997 (2017).
- 15 Kohda, M., Okayasu, T. & Nitta, J. Spin-momentum locked spin manipulation
in a two-dimensional Rashba system. *Sci. Rep.* **9**, 1909 (2019).
- 16 Rendell, M. J. *et al.* Gate voltage dependent Rashba spin splitting in hole
transverse magnetic focusing. *Phys. Rev. B* **105**, 245305 (2022).
- 17 Avsar, A. *et al.* Colloquium: Spintronics in graphene and other two-dimensional
materials. *Rev. Mod. Phys.* **92**, 021003 (2020).
- 18 Taychatanapat, T., Watanabe, K., Taniguchi, T. & Jarillo-Herrero, P.
Electrically tunable transverse magnetic focusing in graphene. *Nat. Phys.* **9**, 225-
229 (2013).
- 19 Lee, M. *et al.* Ballistic miniband conduction in a graphene superlattice. *Science*
353, 1526–1529 (2016).
- 20 Berdyugin, A. I. *et al.* Minibands in twisted bilayer graphene probed by
magnetic focusing. *Sci. Adv.* **6**, eaay7838 (2020).
- 21 Lee, G.-H., Park, G.-H. & Lee, H.-J. Observation of negative refraction of Dirac
fermions in graphene. *Nat. Phys.* **11**, 925 (2015).
- 22 Chen, S. *et al.* Electron optics with p-n junctions in ballistic graphene. *Science*
353, 1522–1525 (2016).
- 23 Miao, F. *et al.* Phase-Coherent Transport in Graphene Quantum Billiards.
Science **317**, 1530–1533 (2007).
- 24 Young, A. F. & Kim, P. Quantum interference and Klein tunnelling in graphene
heterojunctions. *Nat. Phys.* **5**, 222–226 (2009).
- 25 Völkl, T. *et al.* Magnetotransport in heterostructures of transition metal
dichalcogenides and graphene. *Phys. Rev. B* **96**, 125405 (2017).
- 26 Yang, B. *et al.* Strong electron-hole symmetric Rashba spin-orbit coupling in
graphene/monolayer transition metal dichalcogenide heterostructures. *Phys. Rev.*
B **96**, 041409 (2017).
- 27 Ghiasi, T. S., Ingla-Aynés, J., Kaverzin, A. A. & van Wees, B. J. Large
Proximity-Induced Spin Lifetime Anisotropy in Transition-Metal
Dichalcogenide/Graphene Heterostructures. *Nano Lett.* **17**, 7528–7532 (2017).
- 28 Benítez, L. A. *et al.* Strongly anisotropic spin relaxation in graphene–transition
metal dichalcogenide heterostructures at room temperature. *Nat. Phys.* **14**, 303-
308 (2018).
- 29 Wakamura, T. *et al.* Strong Anisotropic Spin-Orbit Interaction Induced in
Graphene by Monolayer WS₂. *Phys. Rev. Lett.* **120**, 106802 (2018).
- 30 Zihlmann, S. *et al.* Large spin relaxation anisotropy and valley-Zeeman spin-
orbit coupling in WSe₂/graphene/h-BN heterostructures. *Phys. Rev. B* **97**,
075434 (2018).
- 31 Tiwari, P. *et al.* Experimental observation of spin–split energy dispersion in
high-mobility single-layer graphene/WSe₂ heterostructures. *npj 2D Mater. Appl.*
6, 68 (2022).

- 32 Kane, C. L. & Mele, E. J. Z_2 Topological Order and the Quantum Spin Hall Effect. *Phys. Rev. Lett.* **95**, 146802 (2005).
- 33 Kane, C. L. & Mele, E. J. Quantum Spin Hall Effect in Graphene. *Phys. Rev. Lett.* **95**, 226801 (2005).
- 34 Tsoi, V. S. Focusing of electrons in a metal by a transverse magnetic field. *JETP Lett.* **19**, 70-71 (1974).
- 35 van Houten, H. *et al.* Coherent electron focusing with quantum point contacts in a two-dimensional electron gas. *Phys. Rev. B* **39**, 8556-8575 (1989).
- 36 Tsoi, V. S., Bass, J. & Wyder, P. Studying conduction-electron/interface interactions using transverse electron focusing. *Rev. Mod. Phys.* **71**, 1641-1693 (1999).
- 37 Groth, C. W., Wimmer, M., Akhmerov, A. R. & Waintal, X. Kwant: a software package for quantum transport. *New. J. Phys.* **16**, 063065 (2014).
- 38 Liu, M.-H. *et al.* Scalable Tight-Binding Model for Graphene. *Phys. Rev. Lett.* **114**, 036601 (2015).
- 39 Wang, L. *et al.* One-Dimensional Electrical Contact to a Two-Dimensional Material. *Science* **342**, 614 (2013).
- 40 Mayorov, A. S. *et al.* Micrometer-Scale Ballistic Transport in Encapsulated Graphene at Room Temperature. *Nano Lett.* **11**, 2396-2399 (2011).
- 41 Eto, M., Hayashi, T. & Kurotani, Y. Spin Polarization at Semiconductor Point Contacts in Absence of Magnetic Field. *J. Phys. Soc. Jpn.* **74**, 1934-1937 (2005).
- 42 Offidani, M., Milletari, M., Raimondi, R. & Ferreira, A. Optimal Charge-to-Spin Conversion in Graphene on Transition-Metal Dichalcogenides. *Phys. Rev. Lett.* **119**, 196801 (2017).
- 43 Usaj, G. & Balseiro, C. A. Transverse electron focusing in systems with spin-orbit coupling. *Phys. Rev. B* **70**, 041301 (2004).
- 44 Laturia, A., Van de Put, M. L. & Vandenberghe, W. G. Dielectric properties of hexagonal boron nitride and transition metal dichalcogenides: from monolayer to bulk. *npj 2D Mater. Appl.* **2**, 6 (2018).
- 45 Kim, M. *et al.* Control of electron-electron interaction in graphene by proximity screening. *Nat. Commun.* **11**, 2339 (2020).
- 46 Han, W., Kawakami, R. K., Gmitra, M. & Fabian, J. Graphene spintronics. *Nat. Nano.* **9**, 794-807 (2014).
- 47 Roche, S. *et al.* Graphene spintronics: the European Flagship perspective. *2D Mater.* **2**, 030202 (2015).
- 48 Avsar, A. *et al.* Gate-tunable black phosphorus spin valve with nanosecond spin lifetimes. *Nat. Phys.* **13**, 888-893 (2017).
- 49 Gmitra, M., Kochan, D., Högl, P. & Fabian, J. Trivial and inverted Dirac bands and the emergence of quantum spin Hall states in graphene on transition-metal dichalcogenides. *Phys. Rev. B* **93**, 155104 (2016).
- 50 Zhumagulov, Y., Frank, T. & Fabian, J. Edge states in proximitized graphene ribbons and flakes in a perpendicular magnetic field: Emergence of lone pseudohelical pairs and pure spin-current states. *Phys. Rev. B* **105**, 205134 (2022).
- 51 Ashcroft, N. W. & Mermin, N. D. *Solid state physics.* (Holt, 1976).

Author Contributions

DKK conceived and supervised the project. MHL supervised the theoretical part carried out by WHK. QR fabricated the samples and performed the measurements, assisted by HX. Some of the data were collected in NW's group with helps from ZY and XF. QR and WHK analyzed the data, and DKK and MHL interpreted them with input from all authors. TT and KW synthesized the hBN crystals. QR, HX, WHK, MHL, and DKK wrote the paper with input from all authors. All authors discussed the results.

Acknowledgements

The work is financially supported by the National Key R&D Program of China (2020YFA0309600) and by the University Grants Committee/Research Grant Council of Hong Kong SAR under schemes of Area of Excellence (AoE/P-701/20), ECS (27300819), and GRF (17300020, 17300521, 17309722). K.W. and T.T. acknowledge support from JSPS KAKENHI (Grant Numbers 19H05790, 20H00354, and 21H05233) and A3 Foresight by JSPS. N.W. acknowledges support from William Mong Institute of Nano Science and Technology. W.-H. K. and M.-H. L. gratefully acknowledge National Science and Technology Council of Taiwan (grant number: MOST 109-2112-M-006-020-MY3) for financial support and National Center for High-performance Computing (NCHC) for providing computational and storage resources.

Supplementary Information

Ballistic transport spectroscopy of spin-orbit-coupled bands in monolayer graphene on WSe₂

Qing Rao^{1#}, Wun-Hao Kang^{2#}, Hongxia Xue¹, Ziqing Ye³, Xuemeng Feng³, Kenji Watanabe⁴, Takashi Taniguchi⁴, Ning Wang³, Ming-Hao Liu^{2*} & Dong-Keun Ki^{1*}

¹Department of Physics, The University of Hong Kong, Pokfulam Road, Hong Kong, China

²Department of Physics, National Cheng Kung University, Tainan 70101, Taiwan

³Department of Physics and Center for Quantum Materials, The Hong Kong University of Science and Technology, Clear Water Bay, Kowloon 999077, Hong Kong, China

⁴National Institute for Materials Science, Namiki 1-1, Tsukuba, 305-0044, Ibaraki, Japan

#Equal contributions.

*Corresponding authors.

Email: minghao.liu@phys.ncku.edu.tw

Email: dkki@hku.hk

1. Sample fabrication

The WSe₂, h-BN and graphene flakes were exfoliated from corresponding crystals onto silicon wafers and examined under an optical microscope. The flakes with suitable thicknesses and surfaces were selected and assembled onto highly doped silicon substrates with 285-nm-thick oxide, following the standard dry pick-up and transfer technique³⁹. After the assembly, the stacks were annealed at 250 °C for 2 hours in a tube furnace in Ar/H₂ forming gas. 1D electrical contacts were fabricated on the annealed sample through a standard electron-beam lithography and reactive-ion etching (CF₄/O₂ mixture gas with flow rates of 5/25 sccm, RF power: 60W), followed by electron beam evaporation of 5 nm Cr and 50 nm Au films. The devices were finally shaped into Hall bars by another electron-beam lithography and reactive-ion etching process.

2. Electrical measurement

Devices were measured in a 1.5 K cryogen-free variable temperature insert (VTI) with a superconducting magnet. The electrical signals were measured by applying a small low-frequency (17.777 Hz) AC current of 0.1–1 μA between the source and drain terminals and measuring the voltage drop between another two probes using a lock-in amplifier (Stanford Research SR830). The low-noise filters and amplifiers were used to detect small TMF signals. The back gate was controlled by Keithley 2004 source-meter.

3. Quantum transport simulation

Current density maps (the inset of **Fig. 1b** and **Fig. S1e**) and conductance spectra (**Fig. 1b**, right) were simulated using Kwant³⁷, an open-source python package for quantum transport simulations based on tight-binding models. To model transport in graphene on TMDCs, we adopt the effective tight-binding Hamiltonian⁴⁹

$$H = H_0 + H_1 + H_R + H_{vZ} + H_{PIA}, \quad (3)$$

where the first two terms are spin-independent and the rest describe spin-orbit couplings of different origins. The first term, $H_0 = \sum_{\langle i,j \rangle, \sigma} t c_{i\sigma}^\dagger c_{j\sigma}$, is composed of nearest-

neighbor kinetic hopping of strength t , and is typically used to describe a spinless graphene lattice. Here, i, j are lattice site indices, σ is the spin index, $c_{i\sigma}^\dagger$ ($c_{j\sigma}$) is the creation (annihilation) operator that creates (annihilates) an electron of spin σ at site i , and $\Sigma_{\langle i,j \rangle}$ sums over site indices that are nearest to each other. Except H_0 , all the rest of the terms in Eq. (3) arise from the effect of the neighboring TMDC lattice. First, the symmetry between the sublattices A and B of the graphene lattice is broken, giving rise to an effective energy difference experienced by electrons on atoms of the two sublattices, which can be described by

$$H_1 = \sum_{i,\sigma} \xi_{o_i} \Delta c_{i\sigma}^\dagger c_{i\sigma},$$

where o_i is the sublattice index of site i , $\xi_{o_i} = +1$ (-1) when $o_i = A$ ($o_i = B$), and Δ characterizes the strength of such a staggered potential energy. The rest of the three terms in Eq. (2) include the Rashba spin-orbit coupling,

$$H_R = \frac{2i}{3} \sum_{\langle i,j \rangle} \sum_{\sigma,\sigma'} c_{i\sigma}^\dagger c_{j\sigma'} \left[\lambda_R (\hat{\mathbf{s}} \times \hat{\mathbf{d}}_{ij})_z \right]_{\sigma,\sigma'},$$

where λ_R the Rashba coupling strength, $\hat{\mathbf{s}} = (\hat{s}_x, \hat{s}_y, \hat{s}_z)$ is a vector of Pauli matrices acting on spin, and $\hat{\mathbf{d}}_{ij}$ is a unit vector pointing from site j to i , the valley-Zeeman term,

$$H_{vZ} = \frac{i}{3\sqrt{3}} \sum_{\langle\langle i,j \rangle\rangle} \sum_{\sigma,\sigma'} c_{i\sigma}^\dagger c_{j\sigma'} \left[\lambda_I^{o_i} v_{ij} \hat{s}_z \right]_{\sigma,\sigma'},$$

where $\Sigma_{\langle\langle i,j \rangle\rangle}$ sums over site indices i, j that are second nearest to each other, the sign factor $v_{ij} = +1$ (-1) when the resulting hopping path is counterclockwise (clockwise), and $\lambda_I^{o_i}$ is the sublattice-resolved valley-Zeeman coupling strength, and finally the pseudospin-inversion-asymmetry term H_{PIA} that does not influence the band structure at K and K' . Neglecting H_{PIA} and setting $\lambda_I^A = -\lambda_I^B = \lambda$ for both sublattices $o_i = A, B$, the eigenenergy of tight-binding model Hamiltonian Eq. (3) is given by⁵

$$E_{\mu,\nu}(k) = \mu \sqrt{(\Delta^2 + \lambda^2 + 2\lambda_R^2 + \hbar^2 v_F^2 k^2) + 2\nu \sqrt{(\lambda_R^2 - \lambda\Delta)^2 + (\lambda^2 + \lambda_R^2)\hbar^2 v_F^2 k^2}}$$

with $\mu, \nu = \pm 1$, whose low- k expansion simplifies to the eigenenergy of Eq. (1) of the main text, which is adopted in several previous studies^{2,4,5,31}. Note that to account for micron-sized graphene systems, we have adopted the scaled tight-binding model³⁸ which is compatible with the spin-orbit coupling terms as remarked in the recent study⁵⁰. All quantum transport simulations presented here are based on the scaling factor $s_F = 8$.

4. Semi-classical ray tracing

In order to check if the absence of the splitting in the second focusing peak (**Fig. 1b** right and **Figs. 2a-c**) is due to the inter-band scattering at the edge, we have employed the semi-classical ray tracing by solving the following equation of motion⁵¹:

$$\begin{cases} \frac{d\vec{v}}{dt} = \frac{1}{\hbar} \vec{\nabla}_{\vec{k}} E(\vec{k}) \\ \frac{d\vec{k}}{dt} = -\frac{e}{\hbar} \vec{v} \times \vec{B} \end{cases},$$

where one can manually add or remove scattering conditions like the inter-band transition at the edge. **Figure S1** shows the results that clearly prove that the absence of the splitting in the second focusing peak is from the mixing of the two bands S_+ and S_- at the sample edge.

5. Discussions on TMF and SdH oscillations

As discussed briefly in the main text, in TMF, the electrons make only half of the cyclotron motion while in SdH oscillations, it needs to make a full circle without losing its phase coherence. This can give rise to several differences in the two phenomena. First, the TMF is more sensitive to the electron scattering than the SdH oscillations as TMF is from the ballistic motion of electrons that can be destroyed by elastic scattering. Thus, in our sample, we could see the splitting in TMF focusing peak only on the hole side where we find higher sample quality while in SdH oscillations we found no obvious differences in both hole and electron side. Second, as electrons need to make a

full cyclotron motion, SdH oscillations probe the total Fermi surface area only, whereas the TMF can probe the partial trajectory along the Fermi surface. This can make a difference when the band structure is shifted in one momentum direction while keeping its area. This might be the reason why the studies on 2DEG with SOC including ours showed different splitting in TMF and SdH. Lastly, the SdH oscillations generally occur at larger magnetic fields than the TMF. This may result in a stronger effect of the Zeeman energy that couples to out-of-plane spin components. It could thus affect the spin-valley Zeeman and Rashba terms in Eq. (1) differently, leading to different band splitting found in our experiment. Nonetheless, the microscopic process that governs TMF and SdH oscillations is different and our study (together with other studies on 2DEG with SOC^{14,16}) shows that it might be important to consider their differences when analysing the relevant experimental results.

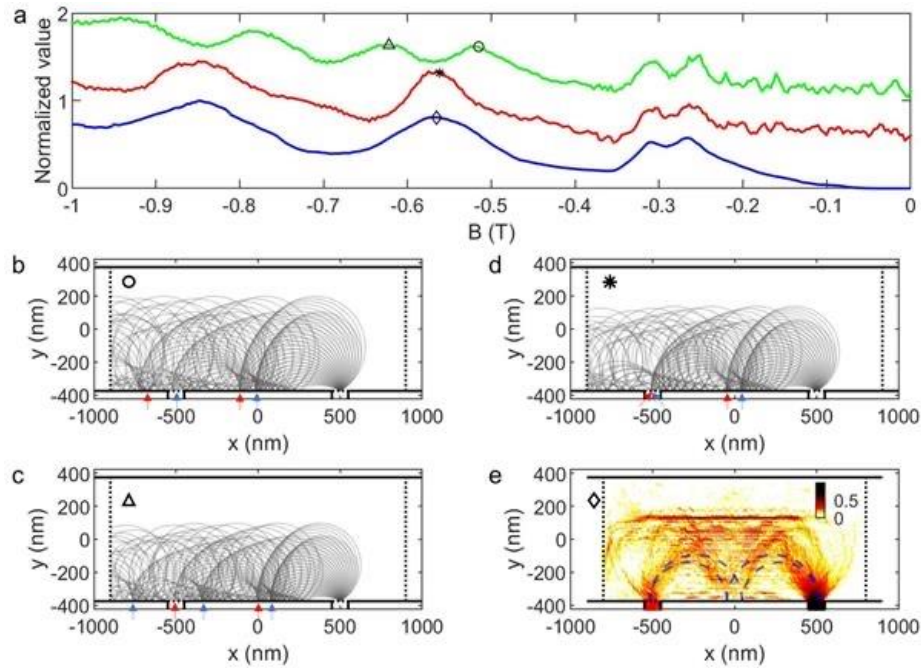


Figure S1. Inter-band transition simulation for the second focusing peak. **a**, Top green and middle red curves: normalized two-point TMF conductance calculated by semi-classical ray tracing without or with inter-band transition, respectively. Bottom blue curve: normalized conductance from quantum transport simulation. As expected, the second focusing peak shows splitting when the inter-band transition is switched off (top green curve). Moreover, the positions of the focusing peaks calculated with inter-band transition (middle red curve) match well with those from Kwant simulation (bottom blue curve), indicating that the observed absence of the splitting in the second focusing peak (**Figs. 2a-c**) is from the inter-band transition. **b-d**, The calculated carrier trajectories at the focusing peaks marked by circle, triangle, and star in **a**, respectively. Red and blue arrows indicate the positions of the scattering at the edge for carriers at S_{\pm} bands, respectively. **e**, Local current density distribution at the focusing peak marked by diamond from quantum transport simulation. Dashed lines illustrate the carrier trajectories.